RSC Advances

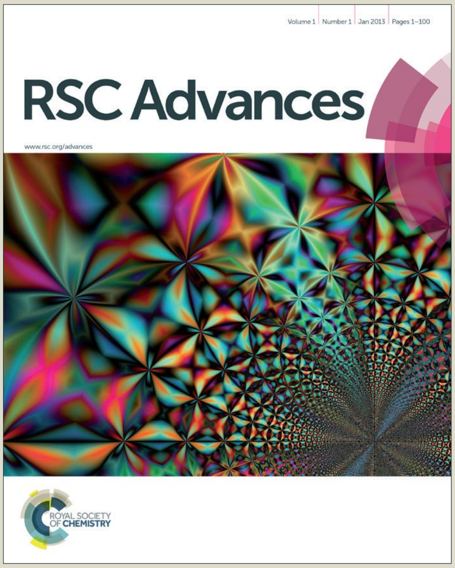

ROYAL SOCIETY OF CHEMISTRY

www.rsc.org/advances

Caterpillar Structured $Ni(OH)_2@MnO_2$ Core/Shell Nanocomposite Arrays on Nickel Foam as High Performance Anode Materials for Lithium Ion Batteries

Ting Wu, Kui Liang[*]

College of Materials Science and Engineering, Hunan University, Changsha 410082, People's Republic of China

ABSTRACT

Caterpillar structured $Ni(OH)_2@MnO_2$ core/shell nanocomposite arrays on nickel foams (CS $Ni(OH)_2@MnO_2$ NFs) are synthesized by a facile hydrothermal method. The nanocomposites consist of $Ni(OH)_2$ nanosheets which are coated by serried ultrathin MnO_2 nanosheets as secondary nanostructure. As anode for lithium ion batteries (LIBs), the as-fabricated CS $Ni(OH)_2@MnO_2$ NFs show improved electrochemical performance, which deliver a high specific capacity of 2223 mAh g^{-1} in the initial discharge process and remain a reversible capacity about 1210 mAh g^{-1} after 80 cycles at 200 mA g^{-1}, corresponding to capacity retention of 74.4% with comparison of the second cycle. CS $Ni(OH)_2@MnO_2$ NFs also show a remarkable rate capability of 650 mAh g^{-1} after 100 cycles while cycling at 1000 mA g^{-1}. The improved electrochemical performance can be ascribed to large surface area, more efficient electrolyte penetration, and multifunctionalities offered by the individual components of the caterpillar core/shell nanostructure. In addition, the self-supported nanocomposite arrays on NFs greatly simplify the fabrication processing of electrodes without applying binder and conductive additive, which provide good electrical contact between the active materials and the substrate. Hence, CS $Ni(OH)_2@MnO_2$ NFs are promising anode candidate for lithium-ion batteries.

KEYWORDS: lithium ion battery; hydrothermal; $Ni(OH)_2$; MnO_2; core/shell

INTRODUCTION

To meet the ever increasing demand in electric vehicles and stationary energy storage applications, developing energy storage devices with high-energy, high-power, long-life, and low-cost, is urgent and important. LIBs have been one of the most popular power sources of continuum energy storage systems.[1-5] LIBs operate by shuttling lithium ions between intercalation host materials, and layered graphite is used as the anode materials. However, graphite negative electrodes have a theoretical capacity of 372 mAh g^{-1}, which cannot fully meet the requirement of high-power systems.[6-8] In this case, various materials have been exploited as the anode materials for LIBs, such as silicon,[9, 10] transition metal hydrides,[11, 12] transition metal hydroxides,[13, 14] and transition metal oxides,[15-20] etc.

Among the candidates, $Ni(OH)_2$ rarely attracts people's attention, because its low electrical conductivity (~10^{-17} S/cm at room temperature) aggravates the fading process especially at high current densities and poor cycling stability which arise from large specific volume variation during the lithium charge/discharge processes.[21] However, $Ni(OH)_2$ also has several advantages such as natural abundance, low cost, low toxicity, higher theoretical capacity than carbon, and superior safety.[22, 23] So, it is meaningful to find an effective way for improving the electrochemical performance of

$Ni(OH)_2$. Two main strategies have been developed to enhance the capacity and structural stability of $Ni(OH)_2$ according to previous work. One strategy is synthesizing nanostructure $Ni(OH)_2$, which can promote electrolyte osmosis and provide large electrode-electrolyte contact region.[24] A. Caballero et al. prepared $Ni(OH)_2$ nanosheets using a high intensity ultrasonic horn method, which showed a high discharge capacity of 1350 mAh g^{-1} after 25 cycles at 100 mA g^{-1}.[13] S. Cabanas-Polo et al. prepared β-$Ni(OH)_2$ nanoplates by electrophoretic deposition， which exhibited a capacity of 600 mAh g^{-1} after 30 cycles at 100 mA g^{-1}.[21] Another strategy is modifying $Ni(OH)_2$ by surface coating or hybridizing with graphene and metals, which can improve conductivity and accommodation of the strain during volume change.[25-28] Baojun Li et al. incorporated reduced graphene oxide into β-$Ni(OH)_2$, which presented a specific discharge capacity of 507 mAh g^{-1} after 30 cycles at 200 mA g^{-1}.[29] Shibing Ni et al. fabricated $Ni(OH)_2$/Ni nanowalls by a novel hydrothermal method, which showed a capacity of 0.59 mAh cm^{-2} after 100 cycles.[28] Nevertheless, materials improved through these methods still face unsatisfactory capacity and cyclic stability, especially at higher current densities. Hence, a more efficient way should be found to improve the electrochemical performance of $Ni(OH)_2$. Currently, it is demonstrated that nanostructured core/shell heterostructures can lead to further enhancement of the capacity and stability.[30-32] MnO_2 with high theoretical capacity (1230 mAh g^{-1}), low cost, and low electromotive force (low potential vs. Li^+/Li) is an appropriate choice for composing core/shell heterostructures with $Ni(OH)_2$ to improve the electrochemical performance.[33, 34]

In this paper, CS $Ni(OH)_2@MnO_2$ NFs were synthesized by hydrothermal method for 6 h. $Ni(OH)_2/MnO_2$ nanocomposite arrays on NFs ($Ni(OH)_2/MnO_2$ NFs) synthesized for 4 h and pure $Ni(OH)_2$ nanosheet arrays on NFs ($Ni(OH)_2$ NFs) were also prepared for comparison. CS $Ni(OH)_2@MnO_2$ NFs exhibited the best electrochemical performance with a first discharge capacity of 2223 mAh g^{-1} and a reversible capacity of 1210 mAh g^{-1} after 80 cycles at 200 mA g^{-1}. This work might prompt us acutely aware of the development potential of transition metal oxides and transition metal hydroxides as LIBs anode materials.

EXPERIMENTAL

Preparation of NF

All of the chemicals used in this experiment were of analytical grade and were used without further purification. The NFs in this work were cut from a large piece of NF with a thickness of 0.5 mm which purchased from Changsha Liyuan new material Co., Ltd. A large piece of NF was carefully cleaned with 2 M HCl solution, deionized water, acetone, and anhydrous ethanol for 15 min in sequence by ultrasound in order to remove the surface oxide layer and other impurities, then drying the NF at 60 ℃. The cleaned NF was cut into circle plate with a diameter of 16 mm and weighed.

Synthesis of $Ni(OH)_2$ NFs

The $Ni(OH)_2$ NFs were prepared by a hydrothermal synthesis method. 1 mmol $Ni(NO3)_2·6H_2O$ (0.29079g), 2 mmol NH_4F (0.07408g), and 4 mmol carbamide (0.24024g) were dissolved in 40 mL deionized water to form a clear solution under magnetic stirring. The mixed solution was transferred into a 50 mL Teflon-lined stainless steel autoclave and the as described NFs were soaked into the solution, after that, the sealed vessel was heated at 120 °C for 4 h before it was cooled to room temperature naturally. The $Ni(OH)_2$ coated NFs were washed with distilled water and ethanol in ultrasound bath for both 10 min, and dried at 60 °C. The reaction for $Ni(OH)_2$ synthesizing could be summarized by the following equations[35, 36]:

$$CO(NH_2)_2 + H_2O \rightarrow NH_3 \cdot H_2O + CO_2 \quad (1)$$

$$NH_3 \cdot H_2O \rightarrow NH_4^+ + OH^- \quad (2)$$

$$Ni^+ + OH^- \rightarrow Ni(OH)_2 \quad (3)$$

Synthesis of CS $Ni(OH)_2$@MnO_2 NFs

$Ni(OH)_2$ NFs and 0.8 mmol $KMnO_4$ (0.1264 g) were transferred into a 50 mL Teflon-lined stainless steel autoclave together with 40 ml deionized water, and maintained at 120 °C for 6 h. When the autoclave cooled down to room temperature, the CS $Ni(OH)_2$@MnO_2 NFs were removed out, and washed with distilled water and ethanol assisted by ultrasound for 10 min, and then dried at 60 °C and weighed again. To investigate the growth process, $Ni(OH)_2/MnO_2$ NFs were also collected at the reaction time of 4 h, and the other conditions were the same as those of the product at 6 h. The reaction for MnO_2 synthesizing could be summarized by the following equation[37]:

$$MnO_4^- \rightarrow MnO_4^{2-} + MnO_2 + O_2 \quad (4)$$

Characterization of $Ni(OH)_2/MnO_2$ nanocomposite arrays on NFs

The as prepared products were investigated by X-ray diffractometer (XRD, Siemens D-5000) with Cu K_α irradiation (λ = 1.5406 Å). The surface morphology of the samples were characterized by scanning electron microscopy (SEM, Hitachi S-4800) and transmission electron microscopy (TEM, JEOL 2010 system operated) with an accelerating voltage of 200 KV.

Electrochemical Measurements of $Ni(OH)_2/MnO_2$ nanocomposite arrays on NFs

All electrochemical measurements were conducted with 2032 coin-type cells. The cells were assembled in the glove box (Super 1220/750, Switzerland) filled with highly pure argon gas (O_2 and H_2O levels less than 0.5 ppm) with the samples without using any binder and conductive additive as the anode, a Li foil as the counter electrode, a microporous polyethylene films (Celgard 2400) as the separator, and a solution of 1 M $LiPF_6$ in ethylene carbonate/dimethyl carbonate/diethyl carbonate (1:1:1, in wt %) as the electrolyte. The mass loading of the active material on NFs was about 2 mg cm^{-2}. The cells were laid for over 12 h before measurement to ensure percolation of the electrolyte into the electrodes. The cyclic voltammetry (CV) and galvanostatic discharge/charge measurement were conducted using a battery testing system (NEWARE BTS-5V 20mA, China) in the voltage of 0.01–3.0 V (vs Li/Li^+). The electrochemical impedance spectroscopy measurements (EIS) were recorded on a CHI660e electrochemical work station at the frequencies ranging from 0.01 Hz to 1 MHz at room temperature.

RESULTS AND DISCUSSION

Figure 1 presents the XRD pattern of CS $Ni(OH)_2@MnO_2$ NFs. The diffraction peaks marked as "★" at 2θ of 19.3, 33.2, 38.6, 52.5, 59 and 62.8 indicate (001), (100), (101), (102), (110) and (111) crystal planes of the $Ni(OH)_2$ (JCPDS, No.14–117). The diffraction peaks marked as "■" at 2θ of 19.2, 37.1, 45.2, 59.8 and 65 can be indexed to (111), (311), (400), (511) and (440) crystal planes of MnO_2 (JCPDS, No.42–1169). And the three strong peaks marked as "●" come from the NF substrate. These conclusions are consistent with the TEM results below.

The SEM images of the pure $Ni(OH)_2$ NFs, $Ni(OH)_2/MnO_2$ NFs and CS $Ni(OH)_2@MnO_2$ NFs are shown in figure 2. Figure 2a reveals that the interlaced $Ni(OH)_2$ nanosheet arrays are self-assembled by some ultrathin $Ni(OH)_2$ nanosheets on the main $Ni(OH)_2$ nanosheets, which form a hierarchical structure with many irregular interspaces. The pure $Ni(OH)_2$ nanosheet arrays have an average length of 500 nm～1 μm. When synthesized the $Ni(OH)_2/MnO_2$ NFs by hydrothermal method in $KMnO_4$ solution for 4 h, many ultrathin MnO_2 nanosheets were uniformly deposited on $Ni(OH)_2$ nanosheets surface (figure 2b). When the reaction time increased to 6 h, more ultrathin MnO_2 nanosheets covered on $Ni(OH)_2$ nanosheets, formed a caterpillar core/shell nanostructure with a width of 400 nm (figure 2c). Figure 2d is the cross-sectional view of the $Ni(OH)_2$ arrays, in which the thickness of the sample is estimated to be 1 μm. The $Ni(OH)_2/MnO_2$ NFs synthesized by hydrothermal method in $KMnO_4$ solution for 10 h is also shown in Figure S1, in which too many MnO_2 nanosheets were covered on $Ni(OH)_2$, and core/shell heterostructures could not be found.

A schematic illustration of the pure $Ni(OH)_2$ NFs, $Ni(OH)_2/MnO_2$ NFs and CS $Ni(OH)_2@MnO_2$ NFs is proposed to clearly understand the growth mechanism, as shown in Figure 3. After treatment of the NF by a hydrothermal route, cross-linked

$Ni(OH)_2$ nanosheet arrays are self-assembled on the NFs . Some MnO_2 nanosheets deposited on $Ni(OH)_2$ nanosheets through another hydrothermal process in $KMnO_4$ solution for 4 h. When the reaction time increased to 6 h, a caterpillar core/shell nanostructure $Ni(OH)_2$@MnO_2 nanocomposite arrays were synthesized, leading to large surface area, more active materials and fast transfer of electron. A possible morphological evolution mechanism can be explained that in order to minimize the overall surface energy, the single MnO_2 nanosheet tends to self-assemble on $Ni(OH)_2$ nanosheet arrays to form caterpillar core/shell nanostructure as the reaction time increased to 6 h.[35]

After the nanocomposite powders were scraped from the NFs and dispersed in ethanol assisted by ultrasound, the CS $Ni(OH)_2$@MnO_2 nanocomposites were examined by TEM and elemental mapping, as shown in Figure 4. In figure 4a, the CS $Ni(OH)_2$@MnO_2 nanocomposite core/shell structure is uniform and well retains after ultrasound bath, in which the $Ni(OH)_2$ nanosheets act as the “core” and the ultrathin MnO_2 nanosheets as the “shell”. Figure 4b shows a lattice-resolution HRTEM of the MnO_2 nanosheets. The spacings are measured to be 0.201 nm, which corresponds to the (400) plane of MnO_2 phase and matches well with the XRD results. The surface scanning element mappings show that O (Figure 4d) and Mn (Figure 4f) elements are homogeneous distributed in the specific portion (Figure 4c) of the CS $Ni(OH)_2$@MnO_2 nanocomposites, while the Ni element (Figure 4e) distributes more in the middle of the sample than the surrounding areas obviously. These results are consistent with the SEM and TEM characterization, that the pure $Ni(OH)_2$ NFs are hierarchical structure with self-assembled by some ultrathin $Ni(OH)_2$ nanosheets on the major $Ni(OH)_2$ nanosheets. And in CS $Ni(OH)_2@MnO_2$ NFs, the MnO_2 nanosheets distribute uniformly on $Ni(OH)_2$ nanosheets.

The electrochemical reactions for the CS $Ni(OH)_2@MnO_2$ NFs nanocomposite arrays could be summarized by the following equations[38, 39]:

$$Ni(OH)_2 + 2Li^+ + 2e^- \leftrightarrow Ni + 2LiOH \qquad (5)$$

$$MnO_2 + 4Li^+ + 4e^- \leftrightarrow Mn + 2Li_2O \qquad (6)$$

The CV curves of the $Ni(OH)_2$ NFs, $Ni(OH)_2/MnO_2$ NFs and CS $Ni(OH)_2@MnO_2$ NFs recorded at 0.3 mV s^{-1} in the potential range of 0.01–3.0 V are shown in figure 5a, c and e, respectively. In the first cathodic process of each electrode, two reduction peaks can be observed at around 0.2 V and 0.8 V. The strong peak at 0.2 V are ascribed to the initial reduction of $Ni(OH)_2$ to Ni, as shown in Eqs. (5). The relatively weak peak at 0.8 V is assigned to the formation of a solid electrolyte interface (SEI) layer[40, 41](figure 5a, c and e) as well as the reduction of Mn^{4+} to Mn^0 (figure 5c and e), as shown in Eqs. (6). As shown in figure 5a, c and e, in the first oxidation process, the peak at around 1.7 V corresponds to the decomposition of the SEI layer,[42,43] and the peak at around 2.3 V can be attributed to the oxidation of Ni to Ni^{2+} and Mn^{2+} to Mn^{4+} (Eqs. (5) and (6)). In addition, figure 5c and e also have a weak peak at around 1.2 V, which corresponds to the reaction of Mn^0 to Mn^{2+}.[30] In the subsequent cycles, the main reduction peak shifted to about 0.7 V and 1.3 V, which may be ascribed to the textural modification. The peak intensity and integral area decrease slightly with the increasing of cyclic numbers.

The galvanostatic charge/discharge curves carried out in the potential window of 0.01–3.0 V at 200 mAh g^{-1} of $Ni(OH)_2$ NFs, $Ni(OH)_2/MnO_2$ NFs and CS $Ni(OH)_2@MnO_2$ NFs are shown in figure 5b, d and f, respectively. The first discharge curve exhibits two voltage plateaus at around 0.23 and 0.75 V of each electrode. In the subsequent discharge processes, these two plateaus shift to around 0.7 and 1.2 V, while the charge plateaus are kept at about 1.6 and 2.3 V. These results are consistent with the CV curves. The first discharge capacity of CS $Ni(OH)_2@MnO_2$ NFs is 2223 mAh g^{-1}, which is much higher than $Ni(OH)_2$ NFs (1468 mAh g^{-1}) and $Ni(OH)_2/MnO_2$ NFs (1885 mAh g^{-1}). The theoretical capacities of $Ni(OH)_2$ and MnO_2 are calculated by the reaction of Eqs. (5) and (6), which are 578 and 1232 mAh g^{-1}, respectively. The excess capacity observed is possibly because of the formation of SEI film and the multifunctionalities offered by $Ni(OH)_2$ and MnO_2.[42-44]

Figure 6a, b and c show the cycling performances of the three samples at 200 mA g^{-1}. It can be seen that the cycling performance of CS $Ni(OH)_2@MnO_2$ NFs is obviously superior to those of $Ni(OH)_2$ NFs and $Ni(OH)_2/MnO_2$ NFs. The first and second discharge capacities of CS $Ni(OH)_2@MnO_2$ NFs are 2223 and 1627mAh g^{-1}, respectively. The initial coulombic efficiency of CS $Ni(OH)_2@MnO_2$ NFs is 68%. It can be attributed to the formation of SEI film which consists of various organic and inorganic compounds such as Li_2CO_3, Li_2O, LiOH and RCO_2Li.[45] After 10 cycles, the coulomb efficiency remains over 97%, the discharge and charge curves almost overlap in the subsequent cycles, indicating enhanced cycling stability. After 80 cycles CS $Ni(OH)_2@MnO_2$ NFs can still maintain a high specific capacities of 1210 mAh g^{-1} (figure 6c). With comparison of the second cycle, the capacity retention for CS $Ni(OH)_2@MnO_2$ NFs is 74.4%, which is much higher than $Ni(OH)_2$ NFs (49.2%) and $Ni(OH)_2/MnO_2$ NFs (56.9%) in figure 6a and b. As shown in figure S2, when cycled at the current density of 1000 mA g^{-1}, CS $Ni(OH)_2@MnO_2$ NFs also showed a superduper capacity. The initial discharge capacity of CS $Ni(OH)_2@MnO_2$ NFs is 1541 mAh g^{-1} and the discharge capacity after 100 cycles is 650 mAh g^{-1}. The outstanding electrochemical performance of CS $Ni(OH)_2@MnO_2$ NFs can attributed to the unique morphological structure. With the increase of the reaction time, more MnO_2 grow on the surface of the $Ni(OH)_2$, forming a caterpillar core/shell nanostructure, which can enhance the capacity and stability. During the cycling process, the MnO_2 nanosheets shell can provide a good structure protection for the inner $Ni(OH)_2$ nanosheets core, and effectively alleviate the volume variation of $Ni(OH)_2$. Meanwhile, $Ni(OH)_2$ nanosheets as the framework can also sustain the MnO_2 nanosheets, ensuring the high effective utilization of large surface-to-bulk ratio of MnO_2 nanosheets. The post-cycling SEM of $Ni(OH)_2$ NFs, $Ni(OH)_2/MnO_2$ NFs and CS $Ni(OH)_2@MnO_2$ NFs after cycling up to 80 cycles at 200 mA g^{-1} are performed in Figure S3. The electrode surface of the CS $Ni(OH)_2@MnO_2$ NFs sample better retains the original structure than the others after cycling, which has no significant cracks and agglomeration, and the active materials still strongly adhere to the substrate. This observation clearly demonstrates that the caterpillar core/shell nanostructure is beneficial for alleviating the structural damage during cycling.

The rate capability of $Ni(OH)_2$ NFs, $Ni(OH)_2/MnO_2$ NFs and CS $Ni(OH)_2@MnO_2$

NFs are shown in figure 6d, e and f, respectively. It is noticeable that the capacities of CS $Ni(OH)_2@MnO_2$ NFs are higher than $Ni(OH)_2$ NFs and $Ni(OH)_2/MnO_2$ NFs at each current density. At the first 10 cycles (100 mA g^{-1}), the average capacities of $Ni(OH)_2$ NFs, $Ni(OH)_2/MnO_2$ NFs and CS $Ni(OH)_2@MnO_2$ NFs are about 1150, 1400, and 1710 mAh g^{-1}, respectively. And at the current density of 1000 mA g^{-1}, the average capacities of $Ni(OH)_2$ NFs, $Ni(OH)_2/MnO_2$ NFs and CS $Ni(OH)_2@MnO_2$ NFs are about 420, 640, and 940 mAh g^{-1}, respectively. When the current reverted to 100 mA g^{-1} after the different high rate charge-discharge cycles, the capacity returned to 807, 1169 and 1580 mAh g^{-1}, corresponding to capacity retention of 70.2%, 83.5% and 92.4% with comparison of the first 10 cycles. The outstanding rate capability of CS $Ni(OH)_2@MnO_2$ NFs can be attributed to the caterpillar core/shell nanostructure. This unique morphological structure with irregular core/shell nanosheet arrays promote the electron transfer and facilitate Li-ion diffusion, meanwhile, help soaking of electrolytes into the electrode materials. Besides, the interspaces between the nanosheet arrays contribute to facile strain relaxation, alleviating the structure damage during the cycling.

Figure 7 shows the AC impedance plots of $Ni(OH)_2$ NFs, $Ni(OH)_2/MnO_2$ NFs and CS $Ni(OH)_2@MnO_2$ NFs electrodes, which are obtained before and after 100 cycles at 1000 mA g^{-1}. The Nyquist plots consist of two semicircles at high and medium frequency regions and an inclined line at low frequency region. The semicircle in high frequency region is related to the SEI film resistance, the semicircle in medium frequency region corresponds charge transfer resistance, and the inclined line in low frequency is due to the lithium ion diffusion process within material.[46, 47] The Nyquist plots are fitted via an equivalent circuit (figure S4), where R_s represents the total resistance of the surface film, electrolyte, and electrical contacts, R_{ct} refers to the charge transfer resistance, W_o is the Warburg impedance related to the diffusion of lithium ions into the bulk materials, and CPE is the constant phase-angle element included the double-layer capacitance.[48] The R_s and R_{ct} value are obtained from the fitting results (table S1). It can be seen that R_s after cycles is little bigger than that before cycles in three samples, which may be due to the formation of SEI film during the cycling. The R_s of CS $Ni(OH)_2$@MnO_2 NFs is higher than that of $Ni(OH)_2$ NFs and $Ni(OH)_2/MnO_2$ NFs after the 100 cycles, suggesting the formation of more stable SEI film in CS $Ni(OH)_2$@MnO_2 NFs. The R_{ct} resistances of all the cells decrease after cycling, and the R_{ct} value of CS $Ni(OH)_2$@MnO_2 NFs electrode is much smaller than $Ni(OH)_2$ NFs and $Ni(OH)_2/MnO_2$ NFs electrodes both before and after the 100 cycles, indicating that CS $Ni(OH)_2$@MnO_2 NFs have a high electrical conductivity and low activation energy for the lithium diffusion.

CONCLUSION

$Ni(OH)_2$ NFs, $Ni(OH)_2/MnO_2$ NFs and CS $Ni(OH)_2$@MnO_2 NFs are synthesized by a facile hydrothermal method. CS $Ni(OH)_2$@MnO_2 NFs exhibit enhanced electrochemical performance than the others, which deliver a high specific capacity of 2223 mAh g^{-1} in the initial discharge process and remain a reversible capacity about 1210 mAh g^{-1} after 80 cycles at 200 mA g^{-1}. The good electrochemical properties of CS $Ni(OH)_2$@MnO_2 NFs can be attributed to the following aspects. First, with the increase of the reaction time, more MnO_2 grow on the surface of the $Ni(OH)_2$, leading to higher capacity. Second, CS $Ni(OH)_2@MnO_2$ NFs present caterpillar core/shell nanostructures, which can enhance the capacity and stability due to larger surface area and more efficient electrolyte penetration. Third, the multifunctionalities offered by $Ni(OH)_2$ and MnO_2 can also enhance the electrochemical properties. During the cycling process, the MnO_2 nanosheets shell can provide a good structure protection for the inner $Ni(OH)_2$ nanosheets core, and effectively alleviate the volume variation of $Ni(OH)_2$. Meanwhile, $Ni(OH)_2$ nanosheets as the framework can also sustain the MnO_2 nanosheets, ensuring the high effective utilization of large surface-to-bulk ratio of MnO_2 nanosheets. Fourth, the self-supported nanocomposite arrays on NFs greatly simplify the fabrication processing of electrodes without applying binder and conductive additive, which provide good electrical contact between the active materials and the substrate. Therefore, the above results indicate that caterpillar structured $Ni(OH)_2@MnO_2$ core/shell nanocomposite arrays on nickel foams are an attractive and promising candidate for LIBs anode electrode.

AUTHOR INFORMATION

Corresponding Authors

*Email: kuiliang@yahoo.com

Notes

The authors declare no competing financial interest.

ACKNOWLEDGMENT

This research work has been financially supported by JiangSu Oliter Energy

Technology Co., ltd.

REFERENCES

1. M. A. a. J.-M. Tarascon, *Nature,* 2008, **451**, 652-657.
2. N. S. Choi, Z. Chen, S. A. Freunberger, X. Ji, Y. K. Sun, K. Amine, G. Yushin, L. F. Nazar, J. Cho and P. G. Bruce, *Angew. Chem. Int. Ed*, 2012, **51**, 9994-10024.
3. Y. S. M. Kisuk Kang, Julien Breger, Clare P. Grey, Gerbrand Ceder, *Science,* 2006, **311**, 977-980.
4. G. Yu, L. Hu, N. Liu, H. Wang, M. Vosgueritchian, Y. Yang, Y. Cui and Z. Bao, *Nano Lett.*, 2011, **11**, 4438-4442.
5. J. B. Goodenough, *Acc. Chem. Res.,* 2013, **46**, 1053-1061.
6. Q. Si, K. Hanai, T. Ichikawa, A. Hirano, N. Imanishi, Y. Takeda and O. Yamamoto, *J Power Sources*, 2010, **195**, 1720-1725.
7. Z. Sun and X. Lu, *Ind. Eng. Chem. Res.*, 2012, **51**, 9973-9979.
8. M. A. J.-M. Tarascon, *Nature*, 2001, **44**, 359-367.
9. Q. Si, M. Matsui, T. Horiba, O. Yamamoto, Y. Takeda, N. Seki and N. Imanishi, *J Power Sources*, 2013, **241**, 744-750.
10. R. N. P. Candace K. Chan, Michael J. O'Connell, Brian A. Korgel, and Yi Cui, *Acs Nano*, 2010, **4**, 1443-1450.
11. Y. Oumellal, A. Rougier, G. A. Nazri, J. M. Tarascon and L. Aymard, *Nat Mater*, 2008, **7**, 916-921.
12. J. Zhang, W. Zaïdi, V. Paul-Boncour, K. Provost, A. Michalowicz, F. Cuevas, M. Latroche, S. Belin, J.-P. Bonnet and L. Aymard, *J. Mater. Chem. A*, 2013, **1**, 4706.
13. A. Caballero, L. Hernán, J. Morales, S. Cabanas-Polo, B. Ferrari, A. J. Sanchez-Herencia and J. Canales-Vázquez, *J Power Sources*, 2013, **238**, 366-371.
14. P. J. S. Xianyou Wang, Ari-Carman Millan, P.V. Parkhutik, S.A. Gamboa, *J New Mat Electr Sys*, 2004, **8**, 101-108.
15. B. Z. Huan Pang, Jimin Du, Jing Chen, Jiangshan Zhang, Sujuan Li, *RSC Adv.,* 2012, **2**, 2257-2261.
16. L. Liu, M. Ge, H. Liu, C. Guo, Y. Wang and Z. Zhou, *Colloids Surf., A: Physicochem. Eng. Aspects,* 2009, **348**, 124-129.
17. L. Liu, Y. Zhao, H. Liu, H.-Z. Kou and Y. Wang, *Nanotechnology*, 2006, **17**, 5046-5050.
18. K. Xie, J. Li, Y. Lai, W. Lu, Z. a. Zhang, Y. Liu, L. Zhou and H. Huang, *Electrochem Commun*, 2011, **13**, 657-660.
19. W. Yao, J. Yang, J. Wang and Y. Nuli, *J Electrochem Soc*, 2008, **155**, A903.
20. M. Wu, J. Gao, S. Zhang and A. Chen, *J Power Sources*, 2006, **159**, 365-369.
21. S. Cabanas-Polo, Z. Gonzalez, A. J. Sanchez-Herencia, B. Ferrari, A. Caballero, L. Hernán and J. Morales, *J. Eur. Ceram. Soc.,* 2015, **35**, 573-584.
22. J. Ji, L. L. Zhang, H. Ji, Y. Li, X. Zhao, X. Bai, X. Fan, F. Zhang and R. S. Ruoff, *Acs Nano*, 2013, **7**, 6237-6243.
23. Y. Tao, C. Jinfei, Y. Tingting and L. Zaijun, *Mater Res Bull*, 2014, **60**, 612-620.
24. Y. F. Yuan, X. H. Xia, J. B. Wu, J. L. Yang, Y. B. Chen and S. Y. Guo, *Electrochem Commun*, 2010, **12**, 890-893.

25. L. Su, Z. Zhou, X. Qin, Q. Tang, D. Wu and P. Shen, *Nano Energy*, 2013, **2**, 276-282.
26. X. Sun, X. Wang, L. Qiao, D. Hu, N. Feng, X. Li, Y. Liu and D. He, *Electrochim Acta*, 2012, **66**, 204-209.
27. J. Zhu, G. Zhang, X. Yu, Q. Li, B. Lu and Z. Xu, *Nano Energy*, 2014, **3**, 80-87.
28. S. Ni, X. Lv, T. Li, X. Yang and L. Zhang, *J. Mater. Chem. A*, 2013, **1**, 1544-1547.
29. B. Li, H. Cao, J. Shao, H. Zheng, Y. Lu, J. Yin and M. Qu, *Chem Commun (Camb)*, 2011, **47**, 3159-3161.
30. K. Qiu, H. Yan, D. Zhang, Y. Lu, J. Cheng, M. Lu, C. Wang, Y. Zhang, X. Liu and Y. Luo, *J Solid State Electr*, 2014, **19**, 391-401.
31. J. Y. Liao, D. Higgins, G. Lui, V. Chabot, X. Xiao and Z. Chen, *Nano Lett*, 2013, **13**, 5467-5473.
32. J. B. Wu, R. Q. Guo, X. H. Huang and Y. Lin, *J Power Sources*, 2014, **248**, 115-121.
33. Y. Li, Q. Zhang, J. Zhu, X.-L. Wei and P. K. Shen, *J Mater Chem A*, 2014, **2**, 3163.
34. Q. Qu, Y. Zhu, X. Gao and Y. Wu, *Adv Energy Mater*, 2012, **2**, 950-955.
35. L. C. Wu, Y. J. Chen, M. L. Mao, Q. H. Li and M. Zhang, *ACS Appl Mater Interfaces*, 2014, **6**, 5168-5174.
36. Juan Xu, Yuanzhu Dong, Jianyu Cao, Bing Guo, Wenchang Wang, Zhidong Chen, *Electrochim Acta,* 2013, **114**, 76– 82
37. Ming Huang, Rui Mi, Hao Liu, Fei Li, Xiao Li Zhao, Wei Zhang, Shi Xuan He, Yu Xin Zhang, *J Power Sources*, 2014, **269**, 760-767.
38. M. Huang, X. L. Zhao, F. Li, L. L. Zhang and Y. X. Zhang, *J Power Sources*, 2015, **277**, 36-43.
39. X. Sun, W. Si, X. Liu, J. Deng, L. Xi, L. Liu, C. Yan and O. G. Schmidt, *Nano Energy*, 2014, **9**, 168-175.
40. X. H. Huang, J. P. Tu, B. Zhang, C. Q. Zhang, Y. Li, Y. F. Yuan and H. M. Wu, *J Power Sources*, 2006, **161**, 541-544.
41. G. W. Hao Liu, Jian Liu, Shizhang Qiao, Hyojun Ahn, *J Mater Chem*, 2011, **21**, 3046-3052.
42. D. Xie, Q. Su, W. Yuan, Z. Dong, J. Zhang and G. Du, *J Phys Chem C*, 2013, **117**, 24121-24128.
43. G. Zhou, J. Ma and L. Chen, *Electrochim Acta*, 2014, **133**, 93-99.
44. C. T. Cherian, J. Sundaramurthy, M. V. Reddy, P. S. Kumar, K. Mani, D. Pliszka, C. H. Sow, S. Ramakrishna and B. V. R. Chowdari, *ACS Appl Mater Interfaces*, 2013, **5**, 9957-9963.
45. Liwei Su, Zhen Zhou, Panwen Shen, *J. Phys. Chem. C,* 2012, **116**, 23974−23980
46. S. G. Mohamed, T.-F. Hung, C.-J. Chen, C. K. Chen, S.-F. Hu and R.-S. Liu, *Rsc Adv*, 2014, **4**, 17230.
47. K. Sheem, Y. H. Lee and H. S. Lim, *J Power Sources*, 2006, **158**, 1425-1430.
48. N. S. Spinner, A. Palmieri, N. Beauregard, L. Zhang, J. Campanella and W. E. Mustain, *J Power Sources*, 2015, **276**, 46-53.

FIGURE CAPTIONS

Figure 1. XRD pattern of CS $Ni(OH)_2@MnO_2$ NFs.

Figure 2. SEM images of (a) $Ni(OH)_2$ NFs, (b) $Ni(OH)_2/MnO_2$ NFs, (c) CS $Ni(OH)_2@MnO_2$ NFs, (d) cross-sectional view of $Ni(OH)_2$ NFs.

Figure 3. Schematic illustration for the pure $Ni(OH)_2$ NFs, $Ni(OH)_2/MnO_2$ NFs and CS $Ni(OH)_2@MnO_2$ NFs

Figure 4. TEM images of CS $Ni(OH)_2@MnO_2$ NFs (a) Low-magnification and (b) high-magnification, (c) TEM image of the portion selected with corresponding elemental mappings of (d) O, (e) Ni, and (f) Mn for CS $Ni(OH)_2@MnO_2$ NFs.

Figure 5. Cyclic voltammograms at a scan rate of 0.3 mV s^{-1} and Charge-discharge curves at a current density of 200 mA g^{-1} for different cycles: (a) and (b) $Ni(OH)_2$ NFs, (c) and (d) $Ni(OH)_2/MnO_2$ NFs, (e) and (f) CS $Ni(OH)_2@MnO_2$ NFs.

Figure 6. Cycling performances of (a) $Ni(OH)_2$ NFs, (b) $Ni(OH)_2/MnO_2$ NFs, (c) CS $Ni(OH)_2@MnO_2$ NFs at 200 mA g^{-1}. Rate properties of (d) $Ni(OH)_2$ NFs, (e) $Ni(OH)_2/MnO_2$ NFs, (f) CS $Ni(OH)_2@MnO_2$ NFs at various current densities.

Figure 7. (a) AC impedance plots for $Ni(OH)_2$ NFs, $Ni(OH)_2/MnO_2$ NFs and CS $Ni(OH)_2@MnO_2$ NFs (a) before and (b) after 100 cycles.

Figure 1

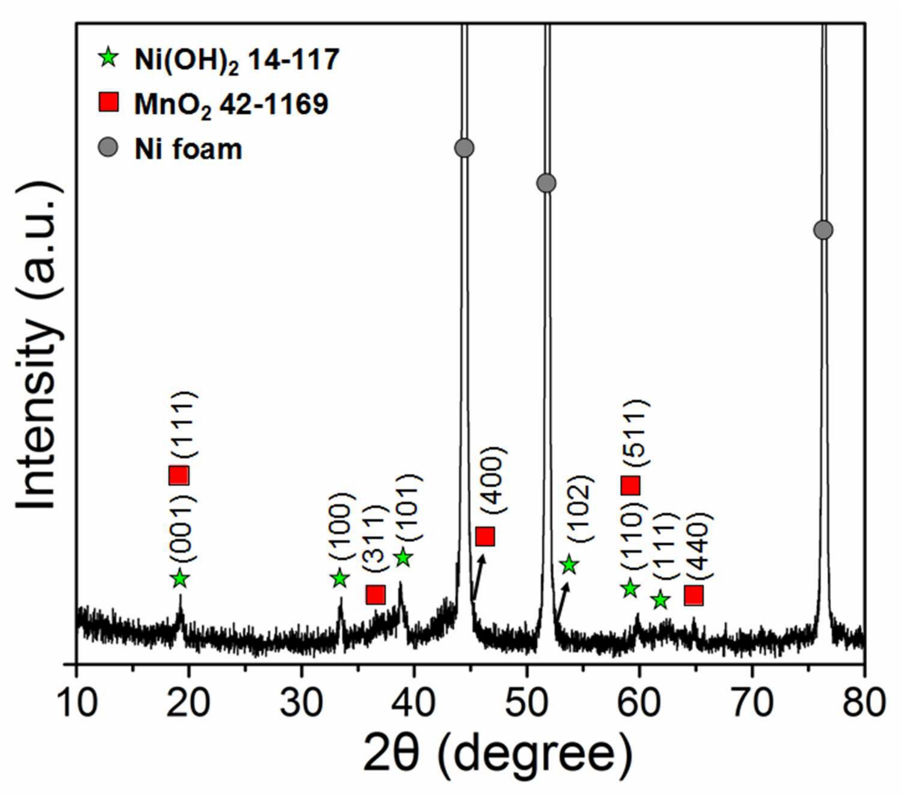
★ Ni(OH)$_2$ 14-117
🟥 MnO$_2$ 42-1169
● Ni foam
Intensity (a.u.)
2θ (degree)
10
20
30
40
50
60
70
80
(001)
(111)
(100)
(311)
(101)
(400)
(102)
(110)
(511)
(111)
(440)

Figure 2

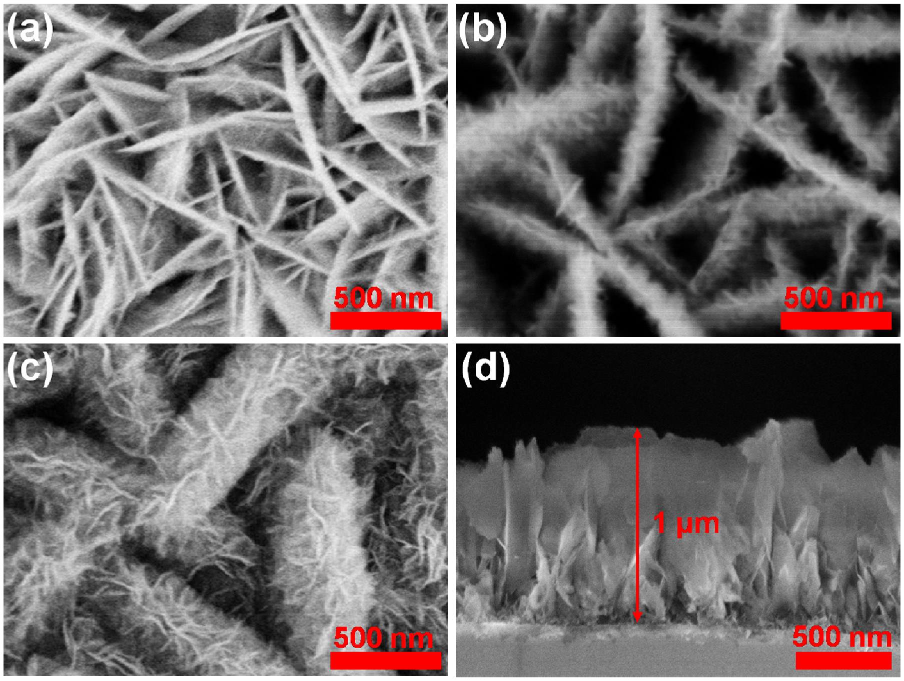

Figure 3

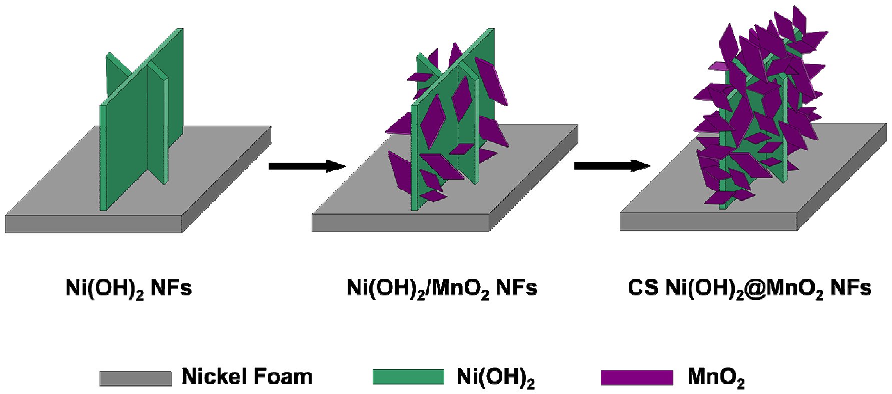
Ni(OH)$_2$ NFs
Ni(OH)$_2$/MnO$_2$ NFs
CS Ni(OH)$_2$@MnO$_2$ NFs
Nickel Foam
Ni(OH)$_2$
MnO$_2$

Figure 4

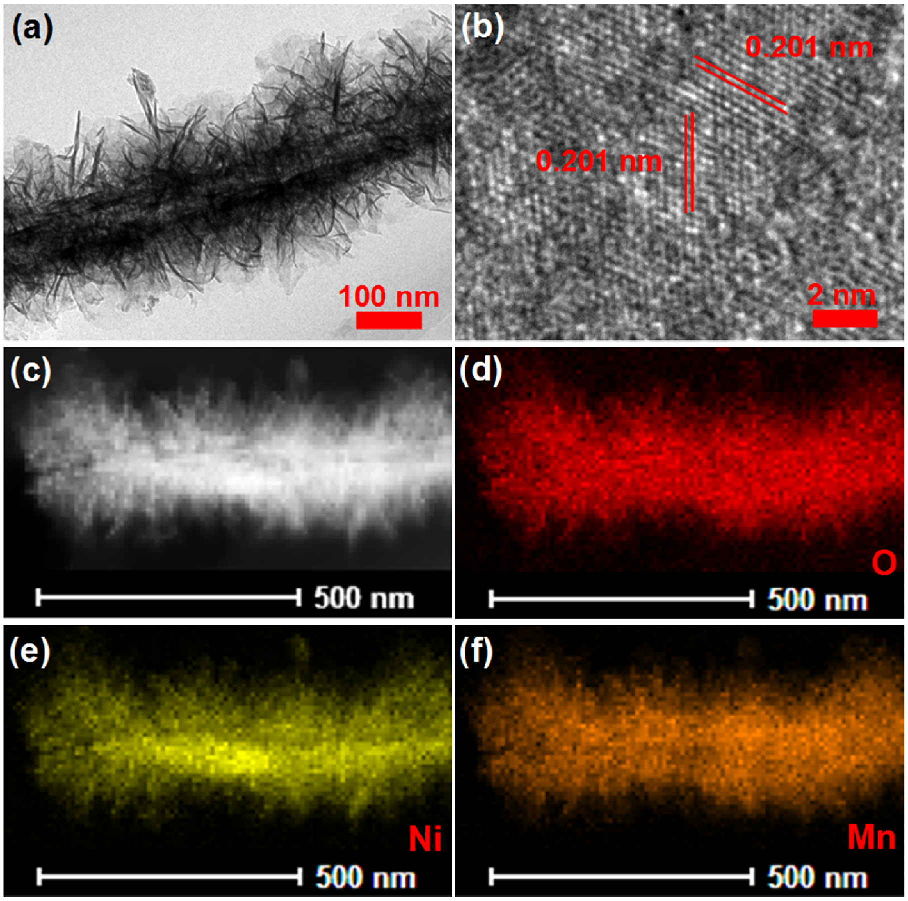
(a)
100 nm
(b)
0.201 nm
0.201 nm
2 nm
(c)
500 nm
(d)
O
500 nm
(e)
Ni
500 nm
(f)
Mn
500 nm

Figure 5

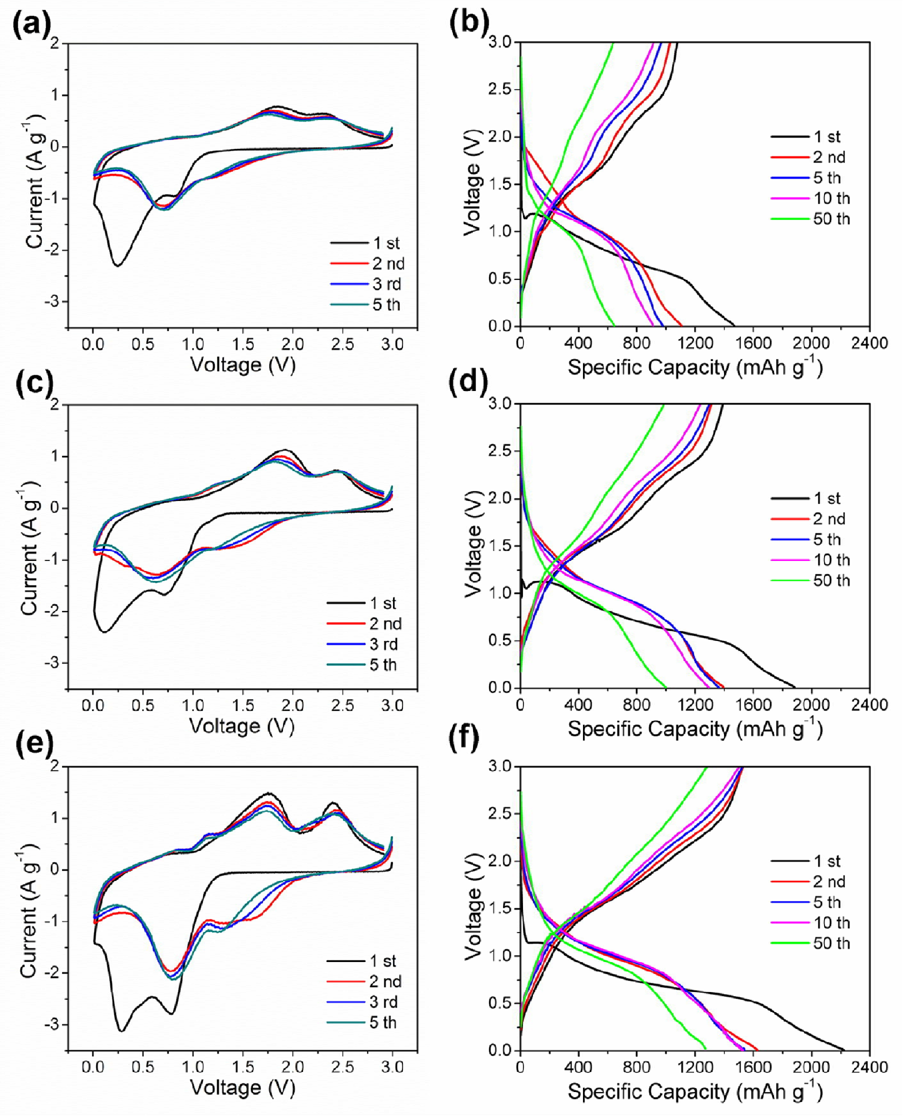
(a)
Current (A g^{-1})
Voltage (V)
1 st
2 nd
3 rd
5 th
(b)
Voltage (V)
Specific Capacity (mAh g^{-1})
1 st
2 nd
5 th
10 th
50 th
(c)
(d)
(e)
(f)
0.0 0.5 1.0 1.5 2.0 2.5 3.0
0 400 800 1200 1600 2000 2400

Figure 6

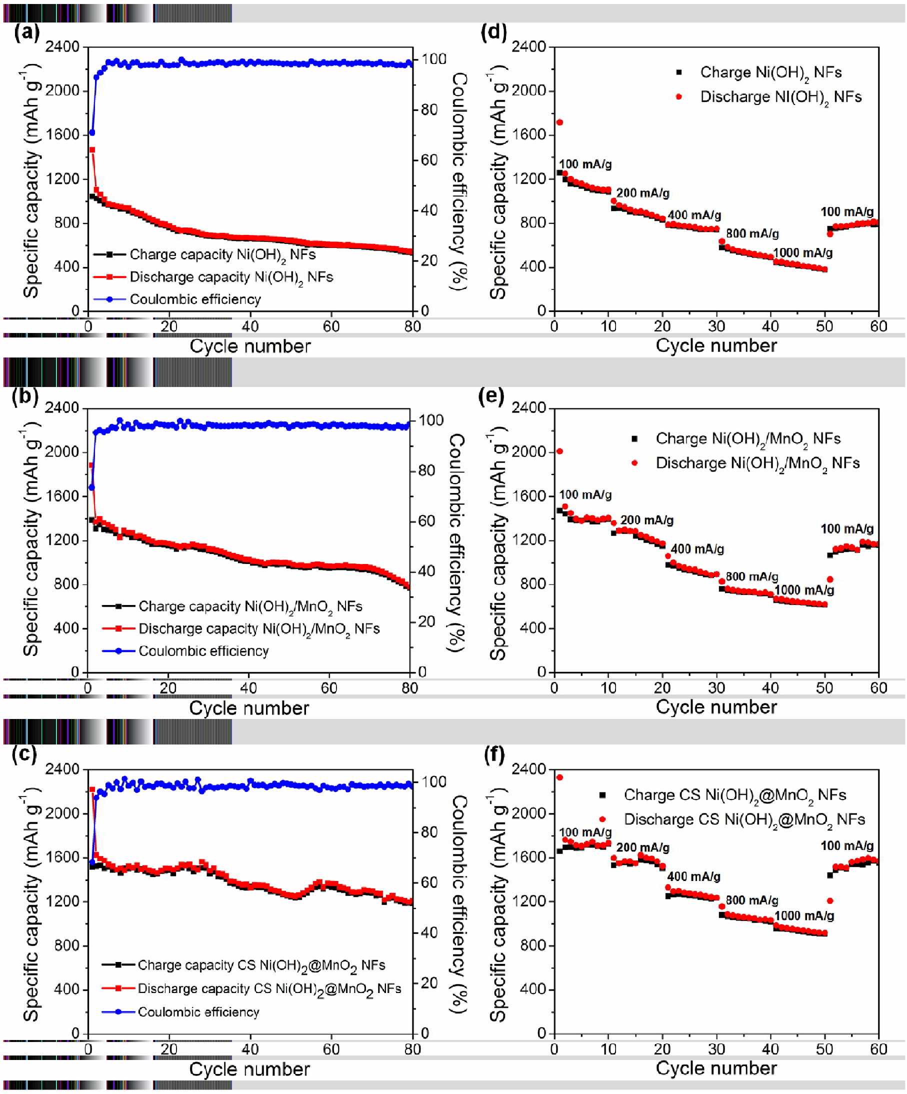
(a)
Specific capacity (mAh g^{-1})
Coulombic efficiency (%)
Cycle number
Charge capacity Ni(OH)$_2$ NFs
Discharge capacity Ni(OH)$_2$ NFs
Coulombic efficiency
(d)
Charge Ni(OH)$_2$ NFs
Discharge NI(OH)$_2$ NFs
100 mA/g
200 mA/g
400 mA/g
800 mA/g
1000 mA/g
100 mA/g
(b)
Charge capacity Ni(OH)$_2$/MnO$_2$ NFs
Discharge capacity Ni(OH)$_2$/MnO$_2$ NFs
Coulombic efficiency
(e)
Charge Ni(OH)$_2$/MnO$_2$ NFs
Discharge Ni(OH)$_2$/MnO$_2$ NFs
(c)
Charge capacity CS Ni(OH)$_2$@MnO$_2$ NFs
Discharge capacity CS Ni(OH)$_2$@MnO$_2$ NFs
Coulombic efficiency
(f)
Charge CS Ni(OH)$_2$@MnO$_2$ NFs
Discharge CS Ni(OH)$_2$@MnO$_2$ NFs
0
400
800
1200
1600
2000
2400
0
20
40
60
80
100
0
10
20
30
40
50
60

Figure 7

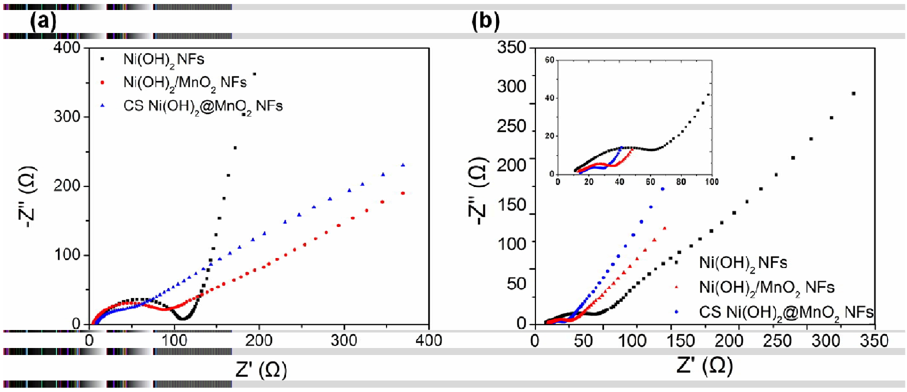
(a)
(b)
Ni(OH)$_2$ NFs
Ni(OH)$_2$/MnO$_2$ NFs
CS Ni(OH)$_2$@MnO$_2$ NFs
-Z'' (Ω)
Z' (Ω)
0
100
200
300
400
0
50
100
150
200
250
300
350
0
20
40
60
80
100

A table of contents entry

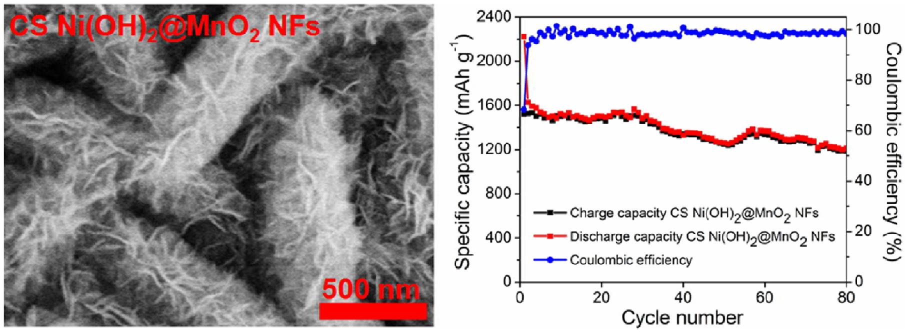

Caterpillar structured Ni(OH)$_2$@MnO$_2$ core/shell nanocomposite arrays on nickel foam as high performance anode materials for lithium ion batteries.